JOURNAL OF GEOPHYSICAL RESEARCH, VOL. 102, NO. C3, PAGES 5583–5594, MARCH 15, 1997

Sea level anomalies in the tropical Atlantic from Geosat data assimilated in a linear model, 1986–1988

L. Gourdeau

Groupe SURTROPAC, Institut Français de Recherche Scientifique pour le Développement en Coopération ORSTOM, Noumea, New Caledonia

J. F. Minster and M. C. Gennero

Unité Mixte de Recherche 39, Groupe de Recherche de Géodésie Spatiale, Toulouse, France

Abstract. Along-track sea level anomalies derived from Geosat altimeter data from November 1986 to November 1988 are assimilated by Kalman filtering into a wind-forced second-baroclinic vertical mode linear model of the tropical Atlantic Ocean. To save computer time, the filter is degraded, mostly by fixing the error covariance matrix of the estimate once the filter has reached its asymptotic behavior. Geosat altimeter data have been processed using improved corrections. The sea surface height variability signal is extracted using the classical along-track technique, relative to a complete reference cycle, and using only tracks longer than 2200 km. This processing has preserved oceanic signals both on large scales (above 1000 km) and on the mesoscale (around 200 km). Sea level anomalies predicted at Principe Island are close to in situ tide gage data, though some differences can be partly related to tidal or orbit error corrections. Oceanographic signals are analyzed from two different sets of fields: one issued from anisotropic space-time objective analysis of Geosat data and the other from the model assimilation. The latter appears as an interesting method to extract low-frequency and propagating signals. Along the equator, eastward propagating features are consistent with Kelvin waves correlated with zonal wind stress anomalies. Upwelling in the Gulf of Guinea is 1 month earlier in 1987 than in 1988. After elimination of the annual and semiannual signals by harmonic analysis, the residual signal over the whole tropical basin, decomposed into complex empirical orthogonal functions, is found dominated by variations between the 2 years, equatorial and tropical signals being anticorrelated.

1. Introduction

Satellite altimeter data provide an unprecedented spatial and temporal coverage to monitor dynamic topography and investigate variations of the ocean circulation. In the tropical Atlantic the seasonal variations of Geosat-derived sea level have been compared to those of dynamic height derived from inverted echo sounders (IES) [*Carton and Katz*, 1990; *Arnault et al.*, 1990], tide gage data [*Arnault and Verstraete*, 1992], and expendable bathythermograph (XBT) data [*Arnault et al.*, 1992a], as well as to dynamic height climatology [*Carton*, 1989; *Arnault et al.*, 1990] and numerical models [*Arnault et al.*, 1990, 1992b; *Didden and Schott*, 1992]. In general, the agreement was quite good in the region of strong sea level signal, i.e., near the North Equatorial Countercurrent (NECC). On the other hand, in the Gulf of Guinea the Geosat-derived sea level signal was much smaller than other estimates. This difference was mostly attributed to data processing [see *Arnault et al.*, 1992b]. Significant improvements of Geosat data corrections have been achieved since, including a relatively precise orbit and better tropospheric corrections [*Cheney et al.*, 1991]. Further efforts have been made to improve some geophysical corrections [*Minster et al.*, 1992a, b]. In addition, the separation of the ocean signal from residual errors can probably be improved using longer satellite tracks as compared to former works.

For most ocean studies, Geosat data need to be interpolated from their space-time satellite sampling into regular grids. This is usually done by objective analysis (OA), which relies on a purely statistical basis and on the definition of a priori covariance functions [e.g., *De Mey and Robinson*, 1987]. Among other interests, data assimilation can be considered as a more sophisticated data interpolation approach which takes into account the laws of ocean dynamics (see *Ghil and Manalotte-Rizzoli* [1991] for a review). In this approach the quality of the interpolation depends both on the model and on the assimilation technique. If the model is too simple, most of the signal contained in the observations will be eliminated, and assimilation will be a poor interpolator. Such experiments may, however, be useful to extract signals of interest from the data [e.g., *Gaspar and Wunsch*, 1989; *Fu et al.*, 1991]. On the other hand, if the model is too complex, assimilation becomes too onerous for simple data interpolation.

Among the various assimilation techniques, Kalman filtering [*Kalman*, 1960] provides an optimal linear estimator of the model state consistent with data and model errors. An important advantage of this technique is in the estimation of error covariances of the filtered signal. It has been investigated by several groups, using Geosat altimeter data and free wave or wind-forced spectral models [e.g., *Gaspar and Wunsch*, 1989; *Fu et al.*, 1991, 1993]. In a preliminary experiment, *Gourdeau et*

Paper number 96JC03245.
0148-0227/97/96JC-03245$09.00

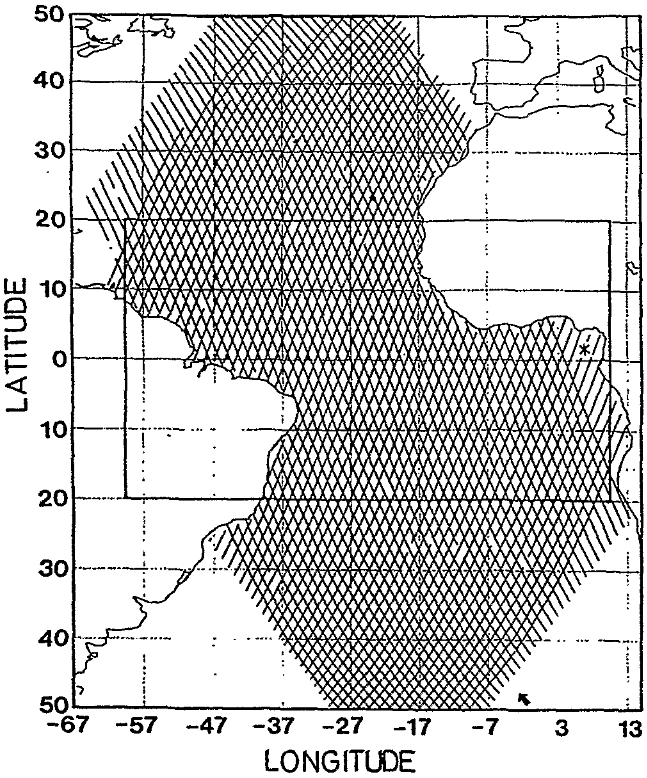

Figure 1. Map of the Geosat tracks used in the analysis. The coverage is that of the reference cycle (cycle 4 from December 29, 1986, to January 15, 1987). The rectangle shows the area for the objective analysis maps (20°N–20°S; 10°E–60°W). The asterisk in the Gulf of Guinea indicates Principe Island.

al. [1992] assimilated, by this technique, 7 months of Geosat sea level anomalies processed by *Arnault et al.* [1992a]. They used a linear model of the tropical Atlantic Ocean [*Arnault et al.*, 1990], which consists of the linearized equations of motion decomposed into vertical modes and forced by wind stress. It was a first attempt of Kalman filtering in such a model that requires a large state vector dimension.

In the present work the model will be extended in space to 20°N and 20°S, in order to give a complete representation of the sea surface in the tropics, and in time from November 1986 to November 1988 when enough of the Geosat Exact Repeat Mission (ERM) data are available. Because of computational cost the assimilation scheme will be degraded, but without giving up either the description of data error or the estimation of the precision of the final estimate. These simplified filters will be tested by comparison with the complete filter. *Fukumori et al.* [1992] and *Fu et al.* [1993] have already demonstrated that steady state Kalman filtering does not necessarily degrade the solution. By comparison with OA we investigate the capacity of the assimilation to extract the low-frequency variability of the tropical Atlantic Ocean. Discussions are principally focused on the less energetic areas such as along the equator and in the Gulf of Guinea, which have been little discussed in former studies.

In the next section of this paper we describe the data processing and mapping through OA. In the third section we comment upon oceanographic results deduced from these maps. Indeed, some equatorial propagations are visible and they are tentatively related to wind forcing. These results are also used for comparison with assimilation results. The following parts concern the assimilation. Section 4 describes the model and the assimilation technique. The results are validated statistically and compared with in situ data in section 5. Predicted oceanographic signals are described in terms of propagating wave-like signals and interannual events in section 6. We conclude in section 7.

2. The Geosat Data

2.1. Along-Track Height Residuals

We used a Geosat ERM data set in which several corrections have been improved as compared to the new T2-Geophysical Data Records (T2-GDR) [*Cheney et al.*, 1991]. They are detailed in Appendix A.

Sea surface height residuals were calculated using the along-track technique [*Ménard*, 1983] but with significant differences compared to former studies. We only kept data belonging to longer than 2200-km arcs (Figure 1). Then, we calculated height residuals relative to an almost complete reference cycle (cycle 4, from January 1 to 16, 1987) rather than relative to the mean along each track; indeed, because of data gaps the estimation of the along-track annual mean is biased along certain tracks, even after reduction of orbit error. The choice of the cycle 4 instead of a mean cycle as the reference has been demonstrated even if residuals relative to cycle 4 are more noisy than those relative to a mean cycle. To decrease the risk of pollution of the results by the orbit error of the reference cycle, we reduced the latter by crossover adjustment between its ascending and descending passes. For each cycle relative to cycle 4, orbit error is described by a bias and tilt for arcs shorter than 6300 km and by a 2° polynomial for longer arcs (in addition to the global orbit error reduction already applied (see Appendix A)). The height residuals were then smoothed along track with a 120-km cutoff wavelength (Lanczos filter).

At this stage of the processing we had 2 years of height residuals relative to the first 2 weeks of January 1987. Along-track wavenumber spectra of our height residuals show a clear-cut break near 120 km (due to the Lanczos filter) and, in general, a continuous red pattern for longer wavelengths, up to more than 1500-km wavelengths. Noise is about 2 cm root-mean-squares (rms).

2.2. Mapping of Sea Level Anomalies Through Objective Analysis

Objective analysis has been used to derive sea level fields from these height residuals. They were obtained using the same OA mapping routine [*De Mey and Robinson*, 1987] as *Arnault et al.* [1992b] and *Didden and Schott* [1992]. This routine is suboptimal in the sense that it selects a limited number of data points (22 on the average, in our case) for each grid point estimate. Space and time autocorrelation functions were defined using outputs of the Laboratoire d'Océanographie Dynamique et de Climatologie (LODYC) three-dimensional (3-D) primitive equation model [e.g., *Reverdin et al.*, 1991]. Along the equator the model has a 0.33° resolution in latitude and on average a 0.75° resolution in longitude; this is compatible with the dynamical ocean features which will be described here, though of course, the model should produce little high-frequency signal, as it is forced with monthly winds. This yielded zonal and meridional decorrelation scales larger than 1000 km and 500 km, respectively. A 15-day temporal decorrelation scale was chosen, in order not to alias high-frequency signals.

The capacity of the mapping routine was tested as follows. The dynamic topography fields derived from the model were subsampled along the Geosat tracks, a 2-cm white noise was added, and the initial signal was reconstructed by OA mapping on a 0.7° longitude and latitude grid. Eighty-eight percent of the variance of the initial signal was recovered. The rms difference between the initial and reconstructed maps was 0.7 cm and did not show the diamond pattern of the Geosat tracks (this was not the case when we used shorter space decorrelation scales). It was also little sensitive to data gaps or isolated missing tracks. For such a noise level, formal error maps were geographically homogeneous around 1 cm.

OA sea level fields were constructed every 10 days. The variance of these maps was 46% of that of along-track height residuals: for comparison, 30% of the variance of the along-track residuals are on shorter than 200-km scales, which have been smoothed by OA. Note also that residual tidal errors should be reduced, as they occur at different apparent phases along crossing tracks. In further discussion we will use sea level anomalies (SLA), obtained from the set of OA maps of height residuals and subtraction of the 2-year average of the OA maps. Space sampling is 2° in longitude and 1° in latitude to be coherent with outputs from assimilation.

3. Variations of Sea Level Anomalies

3.1. Synoptic Maps

Our objective is not to analyze in detail all the signals found in the SLA. We just propose a minimum comparison with former studies. Sea level rms variability was computed for different basin-wide zonal areas characteristic of the tropical Atlantic Ocean (Table 1). They are around twice as large as those computed by *Arnault et al.* [1992b]. The difference on sea level rms variability can be explained by their orbit error reduction on relatively short arcs (between 20°N and 20°S) and by the 140-day temporal decorrelation scale chosen in their objective analysis.

Monthly mean SLA for March, July, and October 1987 are presented on Figure 2. These months are selected for direct comparison with those of *Arnault et al.* [1992b, Figures 14–16]. The maps present classical features of the seasonal evolution of the tropical Atlantic Ocean [e.g., *Merle and Arnault*, 1985]. In March, when the Intertropical Convergence Zone (ITCZ) is close to the equator, high SLA signals are located in the northern hemisphere. At the opposite, in July, when the ITCZ has migrated to the north, high SLA signals are along the equator and south of it, though with a small amplitude. In March the equatorial sea level rise in the Gulf of Guinea is small but extends to about 5°W, while in October it reaches 6 cm close to the eastern coast. In July, upwelling is obvious over most of the Gulf of Guinea.

The qualitative aspects of our maps are very similar to those of *Arnault et al.* [1992b]. However, signals are more zonal, large signals near 20°S and 20°N have disappeared (they were due to border effects), and amplitude in the Gulf of Guinea is quite larger. West of 35°W, in the NECC region, our maps are smoother than those of *Didden and Schott* [1992], though again they are qualitatively similar.

Table 1. Sea Level rms Variability in Different Areas

Area	rms, cm
(14°–16°N), North Equatorial Current (NEC)	5.2
(4°–6°N), North Equatorial CounterCurrent (NECC)	6.3
(2°S–2°N), South Equatorial Current (SEC)	5.1
(4°–6°S), South Equatorial Countercurrent (SECC)	3.4

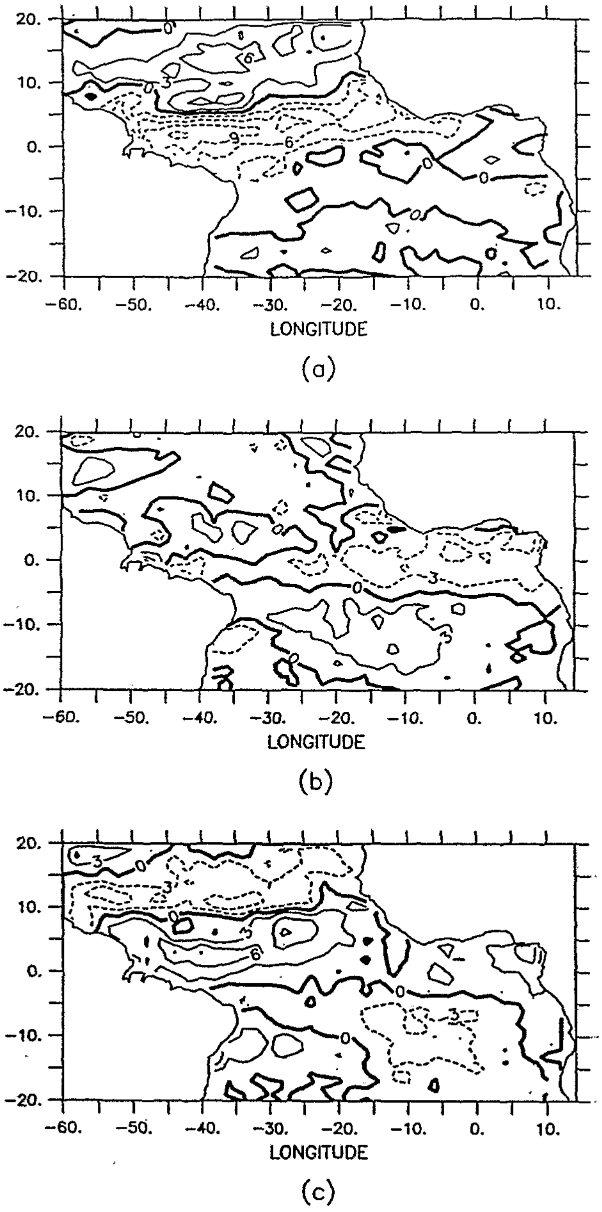

Figure 2. Synoptic OA maps of monthly sea level anomaly from (a) March, (b) July, and (c) October, 1987. Isolines are every 3 cm.

3.2. Comparison With In Situ Data in the Gulf of Guinea

We compared altimetric SLA with tide gage data located at Principe Island (7°30'E, 1°20'N) in the Gulf of Guinea (Figure 1). This region is a critical one for altimetry: due to the geometry of the African coast, satellite tracks can be short, so that most of the signal can be eliminated during orbit error reduction [*Arnault et al.*, 1992a]. Our processing should partly avoid this difficulty, though SLA estimates are mostly derived from

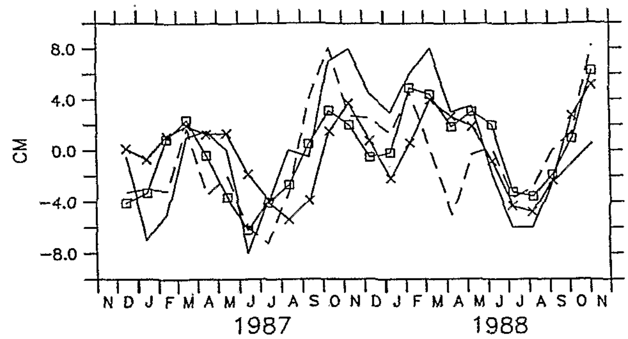

Figure 3. Time series of the sea level anomaly at Principe Island (1.4°N–7.2°E). Solid line, in situ tide gage data; dashed line, altimetric sea level anomaly from the OA maps; solid line with crosses, sea level anomaly from the model; solid line with squares, sea level anomaly from the predicted fields. Units are in centimeters.

descending tracks. Processing of tide gage data is described by *Arnault and Verstraete* [1992]. All values have been referenced to the November 1986 to November 1988 period. Agreement between the two series is good, as they show seasonal signals with very close amplitudes of about 8 cm (Figure 3).

However, SLA series present significant differences from in situ values. In fact, 50% of the variance of the difference can be explained by only two harmonics of 2-cm amplitude and of 120-day and 320-day periods. Both are very small in the in situ data. Both are present in SLA and along-track height residuals, which indicates that they are not an artifact of the OA mapping. Most probably, the second is related to deficiencies of the tidal corrections: indeed, by comparison with the more recent models derived from the TOPEX-POSEIDON data, the *Schwiderski* [1980] model presents errors of the order of 5–10 cm in the Gulf of Guinea. These errors should mostly appear at the 316-day aliased period of the M2 tide, as sampled by the Geosat orbit. Fortunately, this tidal error is large only to the east of 4°E.

The 120-day harmonic seems related to orbit error reduction: it appears between 10° and 35°S in the height residuals of the track near Principe but in phase opposition with its occurrence at Principe. This suggests that it corresponds to an actual subtropical signal, which is partly absorbed by the orbit error reduction and thus aliased at Principe. The minimum in the SLA time series occurring in March–April 1988 (Figure 3) depends on the SLA harmonics. It does not exist in the work by *Arnault and Cheney* [1994], who used the inverse barometer correction in their data processing in contrast to the present processing which is done on very long arcs. The effects of atmospheric pressure are significant out of the tropics and could be at the origin of the 120-day harmonic.

These SLA harmonics are large near Principe, because of the limited amount of data. They do not occur elsewhere, where data from six different tracks are generally used to estimate one OA grid point; indeed, both the phase of tidal errors and the residual orbit errors are different along ascending and descending tracks. Because of this effect, correlation between our SLA series and tide gage data at Principe is 0.59 only. It increases to 0.80 when the two harmonics are subtracted from the SLA signals. The variance of the latter is then 63% of that of the former.

In both altimetric and in situ data the 1987 upwelling signal (low sea level) in the Gulf of Guinea occurs in June–July (Figure 3), i.e., 1 month earlier than in 1988, but with about the same intensity. This 1-month upwelling phase lag between 1987 and 1988 is clearly confirmed on the corresponding SLA maps (not shown). Along the equatorial band (e.g., Figure 2b), the corresponding negative anomaly extends to about 30°W. This difference between the 2 years could result from both the thermodynamic and the wind forcing. Figure 4 shows the time evolution of zonal wind stress anomalies between 1°S and 1°N, as a function of longitude. It indicates that zonal wind intensification west of 25°W occurs 1 month later in 1988 than in 1987, so that it could be the main cause of the sea level difference.

The September–October 1987 high sea level signal at Principe (Figure 3) is mostly confined to the east of 2°E (Figure 2c). Figure 4 suggests that it is correlated with a positive zonal wind anomaly, limited to the eastern coast. Thus, while most of the sea level variations in the Gulf of Guinea seem related to remote events, the September signal is probably due to local wind forcing. This introduces a local semiannual harmonic to the SLA (note though that deep in the Gulf, this harmonic is polluted by tidal errors on S2 and K1, whose aliased periods are close to 180 days).

3.3. Equatorial Signal

Along the equator the dominant SLA signal is annual with out-of-phase variations east and west of about 25°W. The sec-

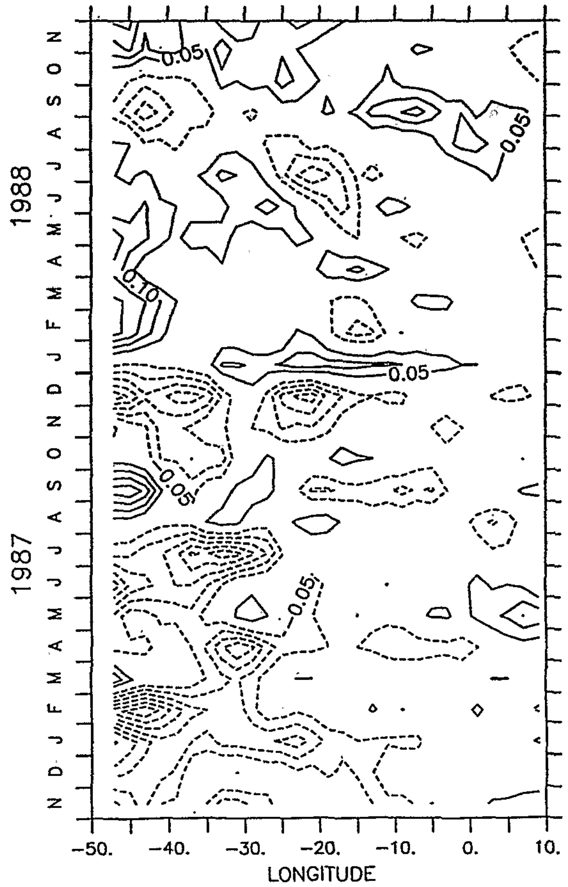

Figure 4. Time plot of the zonal wind stress anomaly, relative to the 2-year mean, averaged between 1°S and 1°N, as a function of longitude. Isolines are every 0.05 N m^{-2}. Dashed lines show negative signals. The zero contour is not drawn.

ond signal in importance is semiannual and particularly present in the east [e.g., *Merle and Arnault*, 1985]. We will not analyze them further as they are relatively well described in the literature. We will rather concentrate on higher-frequency signals. Contrary to the Pacific Ocean, it is difficult to observe propagating equatorial waves in the Atlantic: the timescale for their crossing of this basin is short, their amplitude is small, they are superimposed on the dominant seasonal signal in equilibrium with wind stress, and fluctuations of the wind forcing occur over a large fraction of the basin (e.g., Figure 4). However, first-mode Kelvin waves have been already identified from IES data in the equatorial Atlantic Ocean [*Katz*, 1987].

Low- and high-frequency SLA signals were separated using a 160-day Hanning filter [*Bendat and Piersol*, 1971]. On the low-frequency side, between 1°N and 1°S, we retrieve the annual and semiannual signals of mean amplitude 2.6-cm rms. Evolution of high-frequency signals, averaged between 1°N and 1°S, is presented as a function of time and longitude (Figure 5). They also are at the level of 2.6-cm rms and can be mostly described as coherent structures extending over more than 20° in longitude (more than the zonal decorrelation scale of the OA mapping). They tend to be more frequent in 1988. Their amplitudes are attenuated east of 4°W (this can partly be an effect of the African coast geometry on data processing). They have about 3° latitudinal extension north and south of the equator. Apparently, some of them are propagating eastward and cross the basin in about 1 month. Their apparent phase speeds were estimated at each longitude through a zonal space and time-lag correlation matrix analysis; errors were determined by the rms of the estimations across the basin. The apparent phase speed averages velocities representative of the different effects present in the temporal window and zonal range chosen for the correlation matrix analysis. Positive SLA features will be considered as "downwelling events," and negative SLA features will be considered as "upwelling events." The most significant feature, the downwelling event of January 1988, presents a 2 ± 0.5 m s^{-1} apparent phase speed, suggesting a first-baroclinic-mode Kelvin wave. On the other hand, the upwelling February–March 1988 feature has an apparent phase speed of 1.3 ± 0.3 m s^{-1}, coherent with a second-baroclinic-mode Kelvin wave.

Qualitatively, all these features can be associated with variations of the zonal wind stress shown on Figure 4, easterly wind anomalies for upwelling events and westerly wind anomalies for downwelling events. Except in January 1988 and possibly in October 1988, the wind anomalies do not occur simultaneously over the whole basin. The January 1988 SLA feature started from the western Atlantic at a time of strong wind stress release extending over the whole basin (for comparison this release is much better defined than in 1987). Given the size of the tropical Atlantic basin, the monthly sampling of the wind field does not allow a detailed analysis of the time evolution of this release. In particular, it could trigger a sea level downwelling event at all longitudes and not a single freely propagating Kelvin wave.

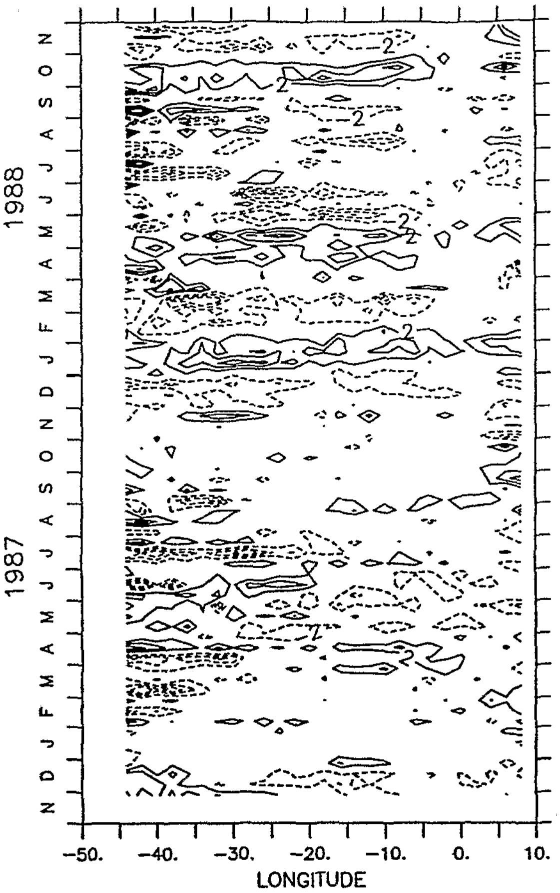

Figure 5. Time plot of the high-frequency sea level anomaly averaged between 1°S and 1°N, as a function of longitude. Isolines are every 2 cm. The zero contour is not drawn.

4. Model and Assimilation Method

4.1. The Model

The model [see *Arnault et al.*, 1990, 1992a] computes the linear response of the tropical Atlantic Ocean to wind forcing through baroclinic modes. Its mesh size is 2° in longitude and 1° in latitude, and the basin extends from 20°N to 20°S and from 60°W to 14°E. The temporal scheme is a leapfrog scheme, with a time step of 4 hours. No-slip boundary conditions have been used along the coasts and the southern and northern boundaries. The model was spun up over 15 years by the monthly wind stress [*Servain and Lukas*, 1990] averaged over the 1985–1988 period, and then run with the 1985–1988 monthly forcing. *Du Penhoat and Tréguier* [1985] have shown that 95% of the signal obtained with nine baroclinic modes was provided by the first three, the second one being dominant [*Busalacchi and Picaut*, 1983; *McCreary et al.*, 1984]. To limit the number of variables for the assimilation problem, only the second vertical baroclinic mode was used (but with 20 meridional modes, this number depending on the size of the domain and the resolution). The decomposition into vertical modes was obtained from a mean density profile, characteristic of the midequatorial Atlantic Ocean (24°W). The phase speed associated with the second-baroclinic-mode Kelvin waves is 1.32 m s^{-1}. Pressure and horizontal velocities were computed at the surface from the linearized equations of movement discretized on a staggered grid.

4.2. The Assimilation Method

The theory of Kalman filtering has been extensively discussed in the literature [e.g., *Kalman*, 1960; *Anderson and Moore*, 1979]. A Kalman filter sequentially provides the estimation of a model state vector (X) by optimal combination of the information contained both in the observations and in the

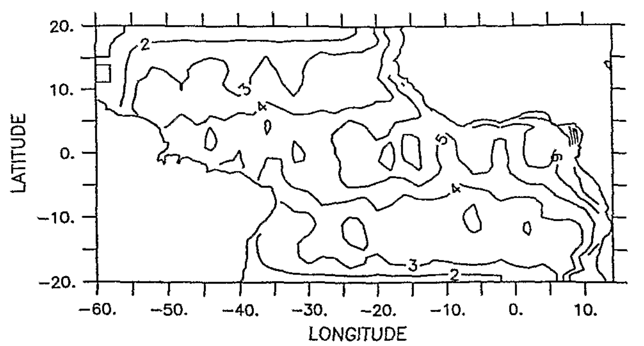

Figure 6. Map of the stationary rms error of the predicted fields. Isolines are every centimeter.

model prediction (by computing a "gain matrix" K). It is a statistical method that requires the definition of model and observation error covariance matrices (Q and R, respectively), together with the evolution of the error covariance matrix (P) of the estimate (X) through the dynamical laws of the model (see Appendix B). The state vector (X) corresponds to pressure and horizontal velocities at each grid point, defined twice because of the leapfrog scheme. Consequences of this leapfrog scheme on assimilation are detailed on Appendix C. Along-track height residuals were assimilated track by track at each 4-hour time step (k) of the model following their time of measurement over the ocean basin. A maximum of three tracks were assimilated at a given time step k. The number of along-track observations was reduced by using one out of three measurements (i.e., every 21 km), so that the dimension of the observation vector assimilated at a given time step was always less than 500. The significant along-track ocean signals are still oversampled by this 42-km data resolution.

Due to the baroclinic character of the tropical ocean, Geosat sea level anomalies (r) can be directly compared with dynamic height anomalies computed from the model. The dynamic height (h_d) is linearly related, within a bias b (which depends on the reference used for the calculation of dynamic height), to the model pressure p_r (i.e., $h_d = ap_r + b$) [e.g., *Du Penhoat and Tréguier*, 1985]. In order to be consistent with Geosat sea level residuals relative to cycle 4, model dynamic height anomalies must be calculated relative to the same period as cycle 4. The dynamic height reference (h_{ref}) for this period was issued from the model without assimilation. Then, Geosat height residuals can be compared to the model values $h_d - h_{\text{ref}}$. As required by the formulation of Kalman filtering, data are linearly related to the model state vector (X) (see Appendix B).

In effect, the "observations" to be assimilated (z) were pseudodynamic heights and resulted from the addition of Geosat sea level anomalies (r) and the local dynamic height reference (h_{ref}) minus the bias (b) (i.e., $z = r + h_{\text{ref}} - b$).

The optimality of the filter depends on the quality of the error covariance matrices (R and Q). One must take into account the measurement errors into R and errors on the forcing of the model into Q. A third term is important and corresponds to the unmodeled physics, present in the observations but not in the model. The error covariance function of the observations (R) was the same as that given by *Gourdeau et al.* [1992]. It is representative of instrumental noise, of residual errors of the satellite orbit (after processing), and of uncertainties in the geophysical corrections. The covariance function was characterized by a 14.5-cm^2 variance and an along-track zero crossing at 800 km (thus R is not diagonal). Each track was considered independent. Following *Miller and Cane* [1989] and *Fu et al.* [1993], the main source of error included in the model error covariance (Q) came from uncertainties on the wind forcing. We defined random wind stress errors from the error covariance function of the wind (defined as in the work by *Miller and Cane* [1989]). Then, the model was run during 1 year using wind stress fields [*Servain and Lukas*, 1990] randomly modified within this error covariance. Model error variances were computed from the difference with the "reference" run. This model error cumulates effects of a 1-year noisy wind stress. As, in principle, Q must represent the error of the model during one time step, these error variances require some adjustment. This adjustment will also take into account the unmodeled error: we used the same empirical approach as *Fukumori et al.* [1992], by describing the unmodeled error as a fraction of the error due to wind stress error. Therefore model error variances defined above were further adjusted by a constant factor, using a trial and error approach, so that the model prediction would explain the greatest part of the signal variance from the observations.

In order to save computer time, we actually applied a suboptimal Kalman filter. The influence of one particular observation is defined by the corresponding column of the gain matrix K. We selected a minimum value under which elements of K were set to zero. This value was fixed at 10^{-2}. In terms of dynamic height anomaly the information brought by such a 10^{-2} gain is 5 orders of magnitude smaller than the predicted anomaly. The analyzed field and its error covariance matrix P were then computed using only the nonzero rows of the gain matrix. Comparisons with the complete calculation during a 1-month period demonstrated that neither the error covariance matrix P nor the variance of the predicted state vector was modified by this truncation. This operation reduced the computational cost, and assimilation of 1 month of data "only" required 3 hours of CPU time on a CRAY 2 computer as compared to the original 20 hours for a state vector dimension of 9348.

The initial state vector X(0) corresponds to the state of the model in November 1986, and the associated error covariance matrix P(0) is initialized using the variance of the initial state. After assimilation of 5 months of data, from November 1986 to March 1987, with the complete filter, the error covariance matrix of the estimate (P) became stationary (when averaged over a period of 17 days corresponding to the cycle of Geosat, so that the data sampling be homogeneous). Then, we fixed P at its stationary value and the steady state filter was run until November 1988. The cost of this final calculation was comparatively very small (30 min for a 1-month data assimilation). It was again verified that the results were unaffected by comparison with the complete calculation during a 1-month period (see also *Fu et al.* [1993]).

5. Statistical Analysis and Comparison With In Situ Data

5.1. Internal Statistics of the Filter

The statistical evaluation of the filter enables us to validate the error covariance matrices, the steady state filter, and the performance of the model solution. The rms error of the predicted sea level (diagonal of matrix P) is shown in Figure 6. The error decreases from 5 cm within the equatorial waveguide to 1–2 cm at the meridional boundaries. This is due to the no-slip boundary conditions and to the Rayleigh friction coefficient of the model, which was artificially increased at the meridional boundaries. This may also reflect equatorial wave dynamics as wave amplitudes are smaller away from the equator. The error increases close to shore in the Gulf of Guinea, in part because of the few Geosat observations available there. Near the northern and southern boundaries, when rms errors are very small, observations have practically no influence on assimilation. For this reason we will only consider the region between 16°N and 16°S. In particular, all spatial averages will be computed inside this domain.

Space covariances of the predicted sea level, as well as between surface pressure and horizontal velocities, have also been analyzed: decorrelation space scales are larger than the a priori value for data errors.

We applied the analysis procedure of *Gaspar and Wunsch* [1989] (see also *Fu et al.* [1991, 1993]). The following parameters were analyzed:

$$E_z = z^T z$$

$$E_t = E_z - \langle e_z^2 \rangle$$

$$U_p = (z - p)^T (z - p)$$

$$U_a = (z - a)^T (z - a)$$

$$E_p = E_t - U_p$$

$$E_a = E_t - U_a$$

Here z and e_z are the assimilated observations and their errors; p and a are the values predicted and analyzed by the filter, respectively (they are pseudodynamic heights as mentioned above); E_z and E_t are the variances of the observations and of the oceanographic signal contained in the observations, respectively; U_p and U_a are the portions of E_z not explained by the prediction and by the analysis, respectively; and E_p and E_a are the portions of E_z explained by the prediction and by the analysis, respectively. The filter is statistically coherent if E_a explains 100% of E_t and $U_p = \langle e_p^2 \rangle + \langle e_z^2 \rangle$, where e_p and e_z are predicted and observation errors, respectively.

All properties are calculated along the satellite tracks. When averaged over the entire observation period, E_z and E_a are 143 and 119 cm^2, respectively. Thus, given the value of $\langle e_z^2 \rangle$, E_a explains 93% of the signal variance of the observations, E_t. But what is the part of variance brought by the altimetric residuals (r)? Recalling that $z = r + c$, where $c = h_{\text{ref}} - b$, E_a can be rewritten as $E_a = \langle r^2 \rangle - U_a + \langle c^2 \rangle + 2\langle rc \rangle$.

Among the 93% of variance explained by the analysis, we found that 50% came from $\langle c^2 \rangle$, 33% came from $\langle r^2 \rangle$, and 10% came from $2\langle rc \rangle$ (Figure 7). So altimetric residuals have contributed for a significant part to the variance of the analysis, as can also be seen by looking at the temporal evolution of these quantities averaged every 17 days. The first statistical criterion for the coherency of the filter is close to being verified except for a 8% loss of the signal variance (10.5 cm^2).

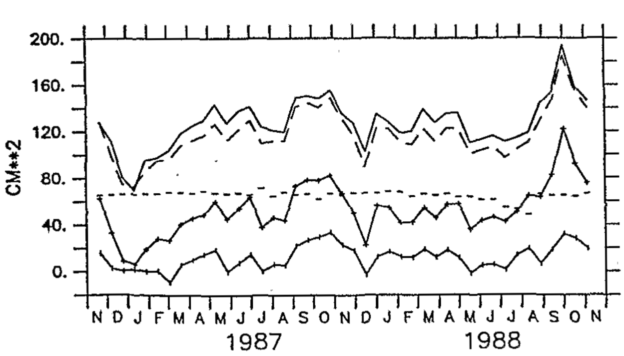

Figure 7. Evolution of the signal variance from the observations (E_t, solid line). The signal variance explained by the analyzed fields (E_a, long-dashed line) is decomposed into explained variance from Geosat anomalies ($\langle r^2 \rangle - U_a$, solid line with crosses), the additive constant ($\langle c^2 \rangle$, short-dashed line), and the covariance between them ($2\langle rc \rangle$, solid line with vertical ticks). Variances are averaged every 17 days. Units are square centimeters.

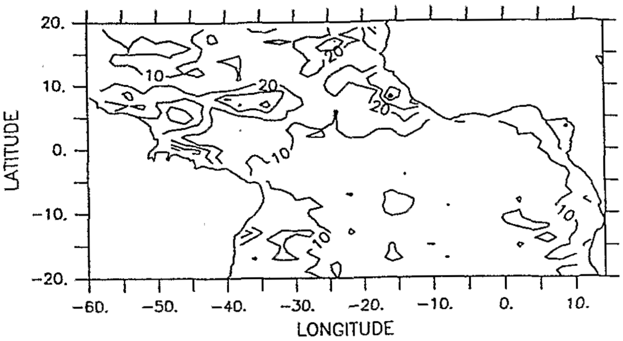

Figure 8. Variance of the difference between OA and prediction averaged over the 2 years. Isolines are every 10 cm^2.

To analyze this "lost" signal, results from the linear model with assimilation were compared to altimetric SLA (Figure 8). Averaged over the domain, the variance of their difference is equal to 12 cm^2 only. Stronger variances are located in nonlinear areas like the shear between the North Equatorial Current (NEC) and the North Equatorial Counter Current and close to the Brazil coast. Differences are not significant everywhere else. The difference between the analyzed fields and the 3-D nonlinear LODYC model showed similar amplitudes (12 cm^2 on the average) and geography. Most probably, the observation signal which was not assimilated in the linear model is due to nonlinear physics contained in the observations and filtered by the model. In principle, this nonlinear physics should have been included in the unmodeled error, but its geography is different from that of the wind-induced model error, which we used for its representation.

For the second criterion we found a 24-cm^2 difference between U_p (55 cm^2) and $\langle e_p^2 \rangle + \langle e_z^2 \rangle$ (16.5 + 14.5 = 31 cm^2). A priori, this result is unsatisfactory. However, because of the grid size of the model (2° longitude by 1° latitude), short wavelength signals can exist in the observations that are filtered out by the model. In order to illustrate this effect, data were smoothed by a 5-point running mean (210-km cutoff wavelength, close to the model grid size). E_a still explained 93% of the signal variance, but U_p was reduced to 41 cm^2.

Figure 9 compares the evolution of U_p (calculated with data filtered along track at 210 km) and $\langle e_p^2 \rangle + \langle e_z^2 \rangle$, averaged every 17 days. On the average, one observes a 12-cm^2 difference between both quantities. It corresponds to the signal variance not assimilated (the 8% of variance lost in E_a) that is not taken into account in the error budget ($\langle e_p^2 \rangle + \langle e_z^2 \rangle$) but contributes to U_p. The difference between U_p and $\langle e_p^2 \rangle + \langle e_z^2 \rangle$ is indeed

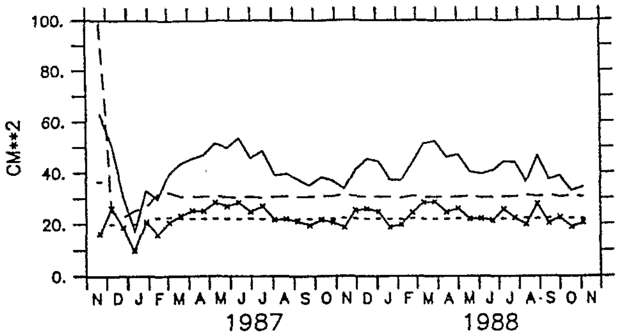

Figure 9. Evolution of error variances of analyzed ($\langle e_a^2 \rangle + \langle e_z^2 \rangle$, short-dashed line) and predicted fields ($\langle e_p^2 \rangle + \langle e_z^2 \rangle$, long-dashed line) and of the portion of the data signal not explained by the analysis (U_a, solid line with crosses) and the prediction (U_p, solid line), averaged every 17 days. Units are square centimeters.

correlated with the variance of the difference between SLA and predicted fields.

The filter is thus found coherent except in limited areas. The assimilation probably filters the nonlinear physics present in the observations, in addition to signals of shorter wavelength than the model resolution. Error covariance matrices should be better defined to take into account more accurately the unmodeled nonlinear physics in specific areas.

5.2. Comparison With Tide Gage Data at Principe Island

As in section 3.2 we compared the assimilated sea level fields and the tide gage data at Principe Island (Figure 3). The model results without assimilation are also presented. Despite a smaller signal than in situ values the latter are reasonably good and do show the semiannual signal. However, they present an important 2-month phase difference with in situ data during the first 8 months. (This difference is also present in the LODYC 3-D model, which suggests that it could be due to the wind forcing, including its monthly resolution).

The predicted state is in good agreement with in situ data and the 1987 upwelling phase lag has disappeared. Even though the signal is quite small relative to error limits (Figure 6), correlation between predicted state and tide gage data is 0.70: the predicted signal is actually closer to in situ data than SLA! No 320-day signal is found in the difference between the predicted state and in situ data, suggesting that local tidal errors have been filtered. Amplitude of the 120-day harmonics is reduced by a factor of 3, compared to SLA. The October 1987 peak is less intense in the prediction (3 cm) than in altimeter or in situ estimates (8 cm). It is interesting to recall that these harmonics were identified as local SLA errors and that the October peak was attributed to a local wind forcing while the other signals seemed remotely forced: this suggests that the assimilated model reproduces large-scale signals more easily than local ones.

6. Oceanographic Results From Assimilation

In this section we analyze some oceanographic signals obtained by assimilation, using the predicted fields (PR). We discuss anomalies relative to the 2-year mean (November 1986 to November 1988). High-frequency and short-wavelength signals in Geosat data have been filtered by the model assimilation, so that the PR fields are a priori more appropriate to study semi-annual, annual, and interannual signals.

6.1. Equatorial Signal

Each observation assimilated in the model creates a pulse that generates Rossby and/or Kelvin waves. The adjustment of the model to the data is achieved through the addition of all these waves. We have analyzed the equatorial signal averaged between 1°S and 1°N using time-longitude and time-latitude plots. Phase speeds of possible propagations have been estimated through the same time-lag correlation matrix analysis as for SLA. A comparison of the plots for the PR and SLA fields indicates that no new signal has been introduced by assimilation. Low- and high-frequency signals have been separated as in SLA (160-day cutoff). Low-frequency PR signals have a 2.3-cm rms amplitude, as compared to 2.6-cm rms for SLA. The semiannual signal in the Gulf of Guinea seems better defined than in SLA.

High-frequency PR signals (Figure 10) are less energetic and less noisy than in SLA (1.5-cm rms). By comparison with Figure 5 the PR fields retrieve the major structures present in SLA, i.e., those extending over a large longitudinal band. Propagations in PR are now clearly visible until the African coast, suggesting that the model transports the new information to the east. On the other hand, local features in the west are filtered out by the assimilation. The most visible propagation

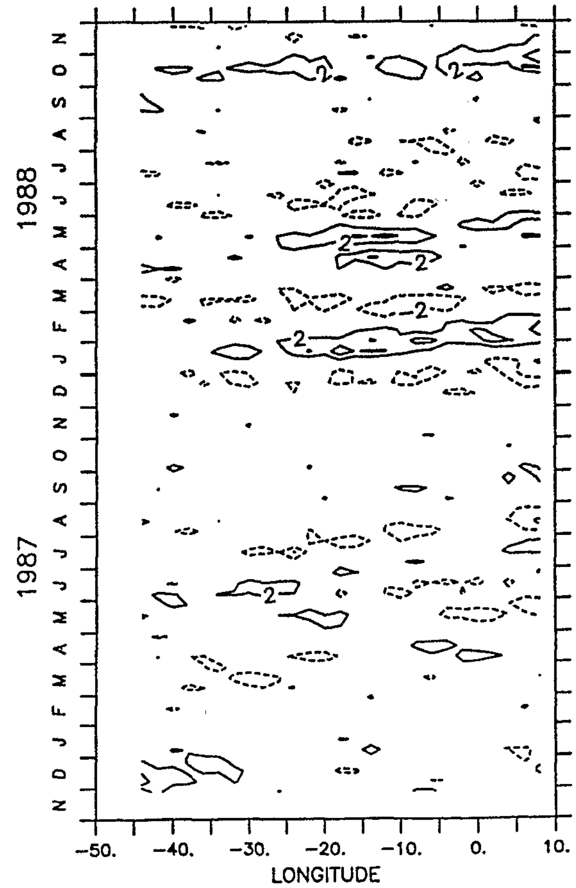

Figure 10. Time plot as a function of longitude of the high-frequency predicted signal averaged between 1°S and 1°N. Isolines are every 2 cm; dotted lines correspond to negative signals. The zero contour is not drawn.

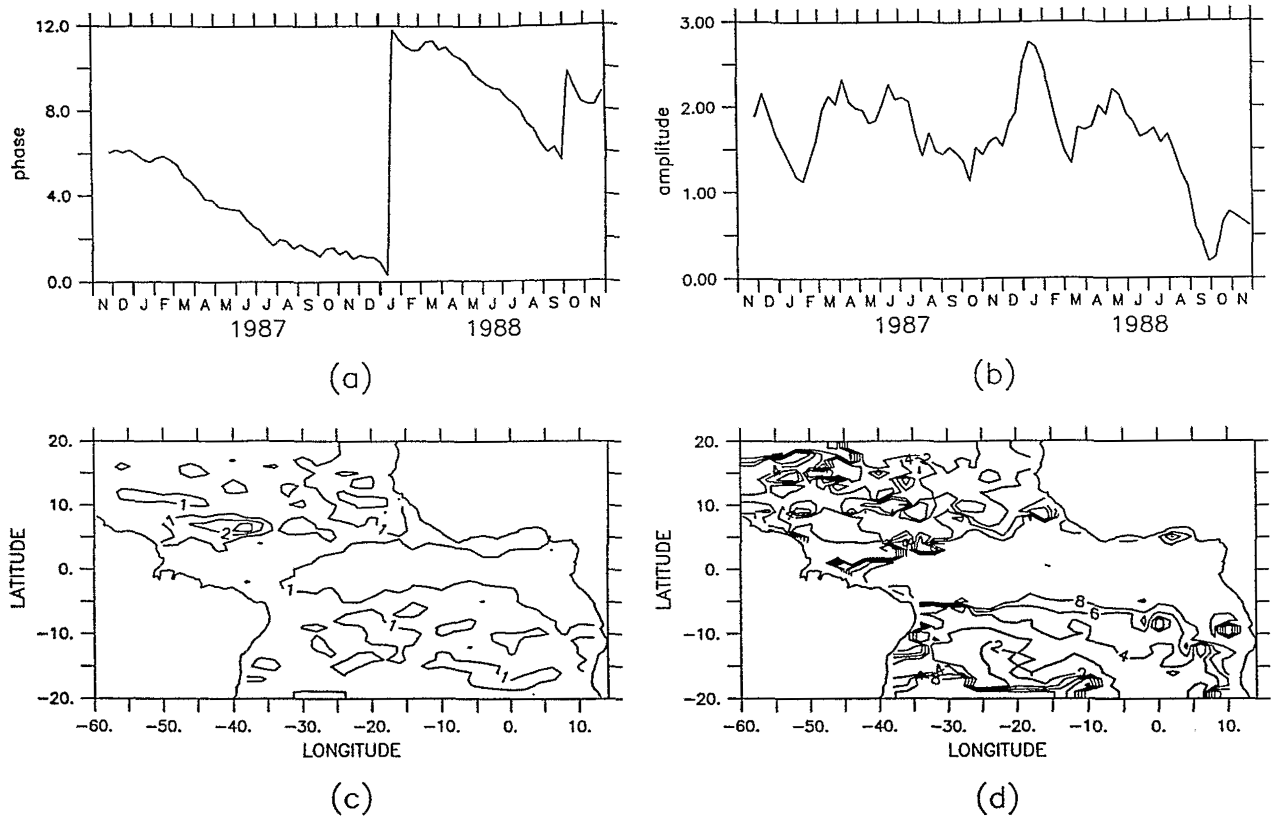

Figure 11. (a) Phase and (b) amplitude evolution and (c) amplitude and (d) phase maps for component 1 of the CEOF decomposition of the predicted fields after elimination of the annual and semiannual harmonics. On Figure 11d the areas anticorrelated with the equatorial waveguide area are shaded. Units for the amplitude maps are normalized. Units of amplitude evolution are centimeters; units of phase are months since January 1987.

signal is the downwelling Kelvin wave-like feature (positive anomaly) in January 1988. Its 2.2 ± 0.5 m s^{-1} apparent phase speed corresponds to a first baroclinic mode, as in SLA. The time-latitude plot indicates that it is centered on the equator, within ±3° latitude. To generate these wave characteristics, the model must create a great number of out-of-phase second-baroclinic-mode Kelvin waves, which sum up to a signal with an apparent velocity close to that of a first baroclinic mode (this may be what actually occurs in reality). In February–March 1988 the upwelling event is characterized by a 1.3 ± 0.25 m s^{-1} phase speed coherent with a second baroclinic mode as in SLA.

6.2. Dominant Structures From CEOF Decomposition

The predicted fields have been decomposed into complex empirical orthogonal functions (CEOF). This allows sorting out, by decreasing variances, of spatial structures that propagate in space and time with frequency modulations [e.g., *Barnett*, 1983]. From the CEOF decomposition of the PR fields we analyzed annual and more particularly interannual signals.

The first component represents 38% of the total variance of the predicted fields (and 18% of the SLA fields) and corresponds to the seasonal evolution of the tropical Atlantic ocean [e.g., *Merle and Arnault*, 1985]. The other components (2 and 3) represent 14 and 10% of the total signal of the predicted fields. They describe a mixture of semiannual and interannual signals and are difficult to analyze.

In order to separate these two last signals, we eliminated the annual and semiannual signals by harmonic analysis at each position. These harmonics correspond to 38 and 11%, respectively, of the signal variance. Then, we analyzed the remaining signal through CEOF decomposition. Component 1 of the latter represents 25% of its variance (and thus 13% of the total signal; note that the sum of the annual and semiannual harmonics and of this CEOF is equal to the sum of the three CEOFs described above). It shows a very regular phase evolution suggesting a quasi-biennial signal (Figure 11a) (though of course, this cannot be deciphered with only 2 years of data). Its amplitude fluctuates until July 1988 before it decreases (Figure 11b). This signal is large in the NECC and in the region of the Guinea dome; along the equator it extends with a nearly constant phase between 5°S and 5°N (Figures 11c–11d).

This CEOF does not permit us to show high-frequency signals, but its maximum amplitudes correspond to the equatorial propagations mentioned above: for example, the amplitude maxima of January and May 1988 (Figure 11b) correspond to the Kelvin-wave-like features (Figure 10). This suggests that a part of this CEOF is due to propagating waves. Indeed, along the equator (i.e., between 1°S and 1°N) the time-longitude plot of the signal reconstructed from this CEOF shows upwelling signals of 3-cm amplitude in March and June 1987 and downwelling signals in January and May 1988 (not shown).

Another representation of this "interannual signal" is obtained from the difference between the years 1988 and 1987. Along the equator this difference shows a band of positive

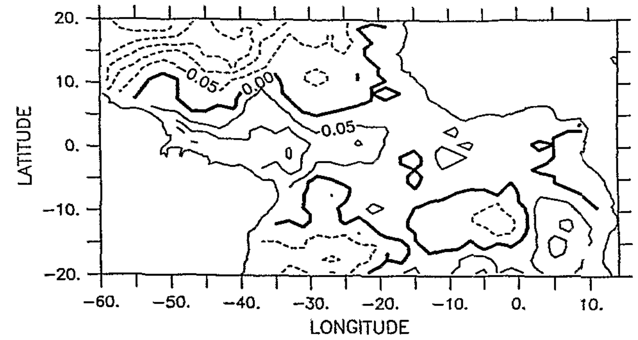

Figure 12. Difference between the mean zonal wind stress of 1988 and 1987. Isolines are every 0.05 N m^{-2}. Dashed contours show negative signals.

signal in both the predicted and OA fields (+2 cm on the average between 4°S and 4°N). The meridional extension of the interannual signal is consistent with that of dynamically trapped waves along the equator. The zonal wind stress difference between 1988 and 1987 (Figure 12) is positive west of 25°W, meaning that the yearly average of the trade winds is less intense in 1988 there. This suggests that the difference between the 2 years takes its origin in the western part of the basin.

Note also the anticorrelation between the equatorial waveguide signal and higher-latitude signal (Figure 11d). As the higher-latitude signal is related to the circulation of the anticyclonic gyre of both hemispheres, this suggests a possible interaction between the equatorial region and the anticyclonic gyres.

7. Conclusions

We have examined high-frequency and interannual variations of the tropical Atlantic Ocean during the November 1986–1988 period with an improved Geosat data set. The effort on the processing of Geosat altimeter data allows a refined description of the sea level signal in the less energetic areas of the domain.

Dynamic height anomalies have first been mapped through objective analysis, using an anisotropic mapping routine. The Geosat signal agrees quite well with in situ tide gage data in the Gulf of Guinea; the difference seems in part due to errors in the tidal or orbit error corrections. Along the equator a strong zonal feature is found in January 1988 (4-cm amplitude), with an apparent phase velocity and a meridional structure consistent with that of a first-mode downwelling equatorial Kelvin wave. It is correlated with a strong release of zonal wind stress across the whole basin. Upwelling in the Gulf of Guinea occurs 1 month earlier in 1987 than in 1988. There the sea level signal seems remotely forced by wind stress in the western Atlantic, except for a 8-cm sea level rise in September–October 1987, which is probably related to a local wind stress anomaly.

Pseudodynamic heights including Geosat along-track height residuals have also been assimilated by Kalman filtering into a simple wind-forced second-baroclinic-mode linear model. Observations have been assimilated along track at their date of measurement, every 21 km between 20°S and 20°N. To save computer time, the filter has been degraded, mostly by fixing the error covariance matrix of the estimate once the filter has reached its asymptotic behavior but also by setting to zero the off-diagonal elements of the gain matrix, when they were smaller than 10^{-2}. The analyzed fields account for 93% of the variance of the along-track pseudodynamic height signal; 33% of this variance comes from Geosat height residuals. The 8% loss of signal variance is located in a few specific areas, where the dynamics is less linear. Everywhere else, the filter can be considered as a mean for constructing sea level anomaly maps consistent with linear equatorial wave propagation and wind forcing. Comparison of the anomalies predicted by the assimilation (PR) with in situ tide gage data at Principe gives a 0.70 correlation coefficient. By comparison with OA results it is found that the model actually accommodates propagating signals whose phase speeds can be different from those of the second-baroclinic vertical mode of the model; in particular, in January 1988 it reproduces quite well a strong feature, whose apparent velocity is comparable with the phase velocity of a first-baroclinic-mode downwelling Kelvin wave.

Decomposition of the predicted fields into complex empirical orthogonal functions shows a dominant annual signal (mode 1; 38% of the total variance). Components 2 and 3 explain together 25% of the total variance. They include a mixture of semiannual and interannual variabilities. After elimination of the annual and semiannual signals by harmonic analysis the residual signal of the predicted fields is dominated by an apparently biennial signal (component 1 of the residuals; 25% of their variance). This signal is in phase opposition between 5°S and 5°N and higher latitudes. A great part of it can be explained by eastward propagating events along the equator that seem generated by wind stress anomalies in the west.

Nowadays, with the high quality of TOPEX/POSEIDON data, more convincing oceanographic results can be expected.. Equatorial propagating waves would be more easily detectable.

Appendix A

We used a data set T2-GDRs with improved corrections. The orbit is that of *Haines et al.* [1990] as in the T2-GDRs. However, the residual orbit error is further reduced by filtering out its main frequencies [*Houry et al.*, 1994].

The wet tropospheric correction has been interpolated from special sensor microwave imager (SSM/I) data by suboptimal mapping, as described by *Minster et al.* [1992a]. This method preserves more of the initial SSM/I water vapor signal in the 200- to 1000-km wave band than the processing used for the T2-GDRs. In addition, we applied a sea state bias correction deduced from the altimeter wind speed and wave height data, using the wind-age formula of *Fu and Glazman* [1991] as adjusted by *Minster et al.* [1992b].

Ocean tidal correction is important because its amplitude is large in this part of the ocean. We used Schwiderski's model [*Schwiderski*, 1980] extended to 16 components by an admittance technique [*Le Provost et al.*, 1991]. In addition, we calculated all the tide load effects from the maps of *Francis and Mazzega* [1990]. We do not include an inverse barometer correction, pressure variations being small in tropical areas.

Appendix B

First, the Kalman filter consists of two predictive equations for the model state vector (X) and its associate error covariance P:

$$\mathbf{X}_p(k) = \mathbf{A}\mathbf{X}_a(k-1) + \mathbf{F}(k-1)$$

$$\mathbf{P}_p(k) = \mathbf{A}\mathbf{P}_a(k-1)\mathbf{A}^T + \mathbf{Q}(k-1)$$

where k denotes time step and subscripts p and a denote model prediction and analysis, respectively, the latter being the best estimate of X combining model forecast with data. A is called the transition matrix which represents the linear equations of the dynamical model. F represents the model forcing by the wind stress, and Q represents the error covariance matrix of the model.

Observations to be assimilated (z) and the state vector of the model (X) must be linearly related:

$$z = \mathbf{H}\mathbf{X}$$

where **H** is an observation matrix with an interpolation scheme that relies on model pressure to the observation z as defined in section 4.2.

Second, the Kalman filter combines the model prediction with the observations to yield an estimate for X and its error covariance P:

$$\mathbf{X}_a(k) = \mathbf{X}_p(k) + \mathbf{K}(k)[z(k) - \mathbf{H}(k)\mathbf{X}_p(k)]$$

$$\mathbf{K}(k) = \mathbf{P}_p(k)\mathbf{H}(k)^T[\mathbf{H}(k)\mathbf{P}_p(k)\mathbf{H}(k)^T + \mathbf{R}(k)]^{-1}$$

$$\mathbf{P}_a(k) = [\mathbf{I} - \mathbf{K}(k)\mathbf{H}(k)]\mathbf{P}_p(k)$$

where **R** is the observation error covariance matrix and **I** is the identity matrix. The matrix **K** is called the gain matrix and determines the weight of observation in modifying model prediction, based on the respective error covariance of the model and the observation.

Appendix C

The leapfrog temporal scheme of the model is an unstable one. At time step k the model computes the prediction of the state at instant $k + 1$ (named $\mathbf{X}(k + 1/k)$) and rectifies the prediction made at instant $k - 1$ to obtain an estimation at instant k (named $\mathbf{X}(k/k)$) through an Asselin filter:

$$\mathbf{X}(k/k) = \mathbf{X}(k/k-1) + 0.01[\mathbf{X}(k-1/k-1) + \mathbf{X}(k+1/k) - 2 \times \mathbf{X}(k/k-1)]$$

Prediction at time step k mostly depends on the estimation at instant $k - 1$ (i.e., $\mathbf{X}(k - 1/k - 1)$). Thus an observation assimilated at time step $k - 1$ on $\mathbf{X}(k/k - 1)$ has little effect at time step k on $\mathbf{X}(k + 1/k)$. If the observation is assimilated on $\mathbf{X}(k - 1/k - 1)$, it has little effect on $\mathbf{X}(k/k)$. So observations are assimilated on both $\mathbf{X}(k/k - 1)$ and $\mathbf{X}(k - 1/k - 1)$ to have a coherent propagation of the information through the temporal scheme of the model [*Gourdeau*, 1991]. Implicitly, we thus consider that observations are not evolving between two time steps of the model (4 hours). While doing so, we double the number of observations operating on the estimation of the state vector at instant k.

Acknowledgments. This work is dedicated to L. Etchegorry, who died prematurely on December 19, 1992. Systematic calculations of the SSM/I water vapor corrections and of the OA maps were his latest contributions. C. Brossier managed the altimeter data. P. Delecluse provided the outputs of the 3-D LODYC model. The assimilation part was initiated while one of us (L.G.) worked under the supervision of J. Merle, S. Arnault, and Y. Ménard. We also benefited from the experience of O. Talagrand. C. Périgaud provided the routine for CEOF decomposition. P. Y. Le Traon, C. Perigaud, R. Hendry, J. Picaut, T. Delcroix, and many scientists from GRGS, CLS-Argos, LODYC, and ORSTOM-Noumea are sincerely thanked for their help and discussions.

References

Anderson, B. D. O., and J. B. Moore, *Optimal Filtering*, 357 pp., Prentice Hall, Englewood Cliffs, N. J., 1979.

Arnault, S., and R. E. Cheney, Tropical Atlantic sea level variability from Geosat (1985–1989), *J. Geophys. Res.*, *99*, 18,207–18,223, 1994.

Arnault, S., and J. M. Verstraete, Rapport préliminaire sur l'utilisation conjointe marégraphes-altimétrie dans le Golfe de Guinée, Rapport au "Programme National d'Etude de la Dynamique du Climat," 24 pp., Cent. Natl. de Rech. Spatiales, Paris, France, 1992.

Arnault, S., Y. Ménard, and J. Merle, Observing the tropical Atlantic Ocean in 1986–1987 from altimetry, *J. Geophys. Res.*, *95*, 17,921–17,945, 1990.

Arnault, S., L. Gourdeau, and J. Merle, Comparison of the altimetric signal with in situ measurements in the tropical Atlantic Ocean, *Deep Sea Res., Part A*, *39*, 481–499, 1992a.

Arnault, S., A. Morlière, J. Merle, and Y. Ménard, Low-frequency variability of the tropical Atlantic surface topography: Altimetry and model comparison, *J. Geophys. Res.*, *97*, 14,259–14,288, 1992b.

Barnett, T. P., Interaction of the Monsoon and Pacific trade wind system at interannual time scales, 1, The equatorial zone, *Mon. Weather Rev.*, *111*, 756–773, 1983.

Bendat, J., and A. Piersol, *Random Data Analysis and Measurement Procedures*, 407 pp., Wiley Interscience, New York, 1971.

Busalacchi, A. J., and J. Picaut, Seasonal variability from a model of the tropical Atlantic Ocean, *J. Phys. Oceanogr.*, *13*, 1564–1588, 1983.

Carton, J. A., Estimates of sea level in the tropical Atlantic Ocean using Geosat altimetry, *J. Geophys. Res.*, *94*, 8029–8039, 1989.

Carton, J. A., and E. J. Katz, Estimates of the zonal slope and seasonal transport of the Atlantic Equatorial Countercurrent, *J. Geophys. Res.*, *95*, 3091–3100, 1990.

Cheney, R. E., W. J. Emery, B. J. Haines, and F. Wentz, Recent improvements in Geosat altimeter data, *Eos Trans. AGU*, *72*, 577, 579–580, 1991.

De Mey, P., and A. Robinson, Assimilation of altimeter eddy fields into a limited area quasi geostrophic model, *J. Phys. Oceanogr.*, *17*, 2280–2293, 1987.

Didden, N., and F. Schott, Seasonal variations in the western tropical Atlantic: Surface circulation from Geosat altimetry and WOCE model results, *J. Geophys. Res.*, *97*, 3529–3541, 1992.

Du Penhoat, Y., and A. M. Tréguier, The seasonal linear response of the tropical Atlantic Ocean, *J. Phys. Oceanogr.*, *15*, 316–323, 1985.

Francis, O., and P. Mazzega, Global charts of ocean tide loading effects, *J. Geophys. Res.*, *95*, 11,411–11,424, 1990.

Fu, L. L., and R. E. Glazman, The effect of the degree of wave development on the sea state bias in radar altimetry measurements, *J. Geophys. Res.*, *96*, 829–834, 1991.

Fu, L. L., J. Vasquez, and C. Perigaud, Fitting dynamic models to the GEOSAT sea level observations in the tropical Pacific Ocean, I, A free wave model, *J. Phys. Oceanogr.*, *21*, 798–808, 1991.

Fu, L. L., I. Fukumori, and N. Miller, Fitting dynamic models to the GEOSAT sea level observations in the tropical Pacific Ocean, II, A linear, wind-driven model, *J. Phys. Oceanogr.*, *23*, 2162–2181, 1993.

Fukumori, I., J. Benveniste, C. Wunsch, and D. B. Haidvogel, Assimilation of sea surface topography into an ocean circulation model using a steady-state smoother, *J. Phys. Oceanogr.*, *23*, 1831–1855, 1992.

Gaspar, P., and C. Wunsch, Estimates from altimeter data of barotropic Rossby waves in the northwestern Atlantic Ocean, *J. Phys. Oceanogr.*, *19*, 1821–1844, 1989.

Ghil, M., and P. Manalotte-Rizzoli, Data assimilation in meteorology and oceanography, *Adv. Geophys.*, *33*, 141–266, 1991.

Gourdeau, L., Application du filtrage de Kalman à l'assimilation de données altimétriques dans un modèle linéaire de l'océan Atlantique tropical, Ph.D. thesis, 270 pp., Univ. Pierre et Marie Curie, Paris, France, 1991.

Gourdeau, L., S. Arnault, Y. Ménard, and J. Merle, Geosat sea-level assimilation in a tropical Atlantic model using Kalman filter, *Oceanol. Acta*, *15*, 567–574, 1992.

Haines, B. J., G. H. Born, G. W. Rosborough, J. G. Marsh, and R. G. Williamson, Precise orbit computation for the Geosat Exact Repeat Mission, *J. Geophys. Res.*, *95*, 2871–2886, 1990.

Houry, S., C. Brossier, K. Dominh, M. C. Gennero, P. Vincent, A. Cazenave, and J-F. Minster, A global Geosat mean sea surface for the year 1987, *J. Geophys. Res.*, *99*, 4519–4533, 1994.

Kalman, R. E., A new approach to linear filtering and prediction problems, *J. Basic Eng.*, *82*, 35–45, 1960.

Katz, E. J., Seasonal response of the sea surface to the wind in the equatorial Atlantic, *J. Geophys. Res.*, *92*, 1885–1893, 1987.

Le Provost, C., F. Lyard, and J-M. Molines, Improving ocean tide predictions by increasing the number of semidiurnal constituents, *Geophys. Res. Lett.*, *18*, 845–848, 1991.

McCreary, J. P., J. Picaut, and W. Moore, Effect of annual remote forcing in the eastern tropical Atlantic, *J. Mar. Res.*, *42*, 45–81, 1984.

Ménard, Y., Observation of eddy fields in the northwest Pacific by Seasat altimeter data, *J. Geophys. Res.*, *88*, 1853–1866, 1983.

Merle, J., and S. Arnault, Seasonal variability on the surface dynamic topography in the tropical Atlantic Ocean, *J. Mar. Res.*, *43*, 267–288, 1985.

Miller, R. N., and M. A. Cane, A Kalman filter analysis of sea level height in the tropical Pacific, *J. Phys. Oceanogr.*, *19*, 773–790, 1989.

Minster, J-F., D. Jourdan, E. Normant, C. Brossier, and M. C. Gennero, An improved SSM/I water vapor correction for Geosat altimeter data, *J. Geophys. Res.*, *97*, 17,859–17,872, 1992a.

Minster, J-F., D. Jourdan, C. Boissier, and P. Midol-Monnet, Estimation of the sea state bias in radar altimeter Geosat data from examination of frontal systems, *J. Atmos. Oceanic Technol.*, *9*, 174–187, 1992b.

Reverdin, G., P. Delecluse, C. Levy, P. Andrich, A. Morlière, and J. M. Verstraete, The near surface tropical Atlantic in 1982–1984: Results from a numerical simulation and a data analysis, *J. Phys. Oceanogr.*, *27*, 273–340, 1991.

Schwiderski, E. W., On charting global ocean tides, *Rev. Geophys.*, *18*, 243–268, 1980.

Servain, J., and S. Lukas, *Climatic Atlas of the Tropical Atlantic Wind Stress and Sea Surface Temperature: 1985–1989*, Cent. Orstom de Brest, Inst. Fr. de Rech. pour l'Exploit. de la Mer, Plouzané, France, *1990.*

M. C. Gennero and J. F. Minster, Unité Mixte de Recherche 39, Groupe de Recherche de Géodésie Spatiale, 18 Avenue E. Belin, 31055 Toulouse, France.

L. Gourdeau, Groupe SURTROPAC, Institut Français de Recherche Scientifique pour le Développement en Coopération (ORSTOM), BP A5, Noumea, 98848 New Caledonia. (e-mail: gourdeau@noumea.orstom.nc)

(Received May 22, 1995; revised October 6, 1996;
accepted October 18, 1996.)